

# Supplementary Information for Dynamic Hovering for Uncrewed Underwater Vehicles via An Error-Separation-based Cooperative Strategy

Xiaoli Luan<sup>1</sup>, Shenhan Yu<sup>1</sup>, and Haiying Wan<sup>1,\*</sup>

<sup>1</sup>the Key Laboratory of Advanced Control for Light Industry Processes. Ministry of Education, Jiangnan University, Wuxi 214122, China

\*whywan@jiangnan.edu.cn

## ABSTRACT

Provide with some supplementary information for "Dynamic Hovering for Uncrewed Underwater Vehicles via An Error-Separation-based Cooperative Strategy", including more experiments under stable ocean current, increasing current disturbance, load-changing cases and prerequisites of LQR, SMC.

## S.1 Specific details of the UUV model

It is a common practice to choose a second-order model to describe the dynamics and kinematics of a streamlined AUV<sup>1</sup>. The six-degree-of-freedom nonlinear dynamic model initially established by<sup>1,2</sup> and other references, along with the traditional parameter acquisition methods (such as drag tank experiments and CFD simulations), are disadvantageous due to their time and cost. To simplify the model, references<sup>1,3-5</sup> employ a second-order model as a substitute for the full model in controller design; however, these approaches have not been rigorously demonstrated<sup>1</sup>. Subsequently, based on the pitch-axes dynamics framework proposed in<sup>8</sup>, the dynamic differences between the full model and the second-order simplified model were analyzed. It was demonstrated that the output feedback controller designed using the second-order model can still ensure the asymptotic stability of the actual system. Consequently, we present the following kinetic model, derived from the second-order model:

$$\begin{cases} \mathbf{v}_{k+1} = -\{\mathbf{M}(\mathbf{v}_k)^{-1}[\mathbf{C}(\mathbf{v}_k)\mathbf{v}_k + \mathbf{D}(\mathbf{v}_k)\mathbf{v}_k + \mathbf{g}(\boldsymbol{\eta}_k)] + \mathbf{M}(\mathbf{v}_k)^{-1}(\boldsymbol{\tau}_{\delta,k} + \boldsymbol{\delta}_k)\}dt + \mathbf{v}_k, \\ \boldsymbol{\eta}_{k+1} = [\mathbf{J}(\boldsymbol{\eta}_k)\mathbf{v}_k]dt + \boldsymbol{\eta}_k, \end{cases} \quad (1)$$

where the terms have the same meaning as defined in the paper. For clarity, we restate these definitions in Remark 1.

**Remark 1**  $dt$  represents the sampling time, determined by the hardware requirements, and  $k$  denotes the discrete time index.  $\mathbf{v}_k$ ,  $\mathbf{v}_{k+1}$ , and  $\boldsymbol{\eta}_k$ ,  $\boldsymbol{\eta}_{k+1}$  represent the velocity vector  $\mathbf{v}$  and the orientation vector  $\boldsymbol{\eta}$  at time steps  $k$  and  $k+1$ , respectively.  $\boldsymbol{\tau}_{\delta,k}$  and  $\boldsymbol{\delta}_k$  denote the control input and the current disturbance at time step  $k$ . The matrices  $\mathbf{M}(\mathbf{v}_k)$ ,  $\mathbf{C}(\mathbf{v}_k)$ ,  $\mathbf{D}(\mathbf{v}_k)$ ,  $\mathbf{g}(\boldsymbol{\eta}_k)$ , and  $\mathbf{J}(\mathbf{v}_k)$  represent the corresponding functions of  $\mathbf{v}_k$  and  $\boldsymbol{\eta}_k$  in the discrete-time model.

Next we show the details in the above model 1. The inertia matrix  $\mathbf{M}(\mathbf{v})$  including the additional mass is

$$\mathbf{M}(\mathbf{v}) = \mathbf{M}_{ad}(\mathbf{v}) + \mathbf{M}_{rbd}(\mathbf{v}), \quad (2)$$

where the  $\mathbf{M}_{ad}(\mathbf{v})$  is the hydrodynamic inertia matrix and  $\mathbf{M}_{rbd}(\mathbf{v})$  is the rigid body inertia matrix, with each has the expression as:

$$\mathbf{M}_{ad}(\mathbf{v}) = \begin{bmatrix} m & 0 & 0 & 0 & mz_g & 0 \\ 0 & m & 0 & -mz_g & 0 & 0 \\ 0 & 0 & m & 0 & 0 & 0 \\ 0 & -mz_g & 0 & I_x & 0 & 0 \\ mz_g & 0 & 0 & 0 & I_y & 0 \\ 0 & 0 & 0 & 0 & 0 & I_z \end{bmatrix}, \mathbf{M}_{rbd}(\mathbf{v}) = \begin{bmatrix} X_{ud} & 0 & 0 & 0 & X_{qd} & 0 \\ 0 & Y_{vd} & 0 & Y_{pd} & 0 & Y_{rd} \\ 0 & 0 & Z_{wd} & 0 & Z_{qd} & 0 \\ 0 & K_{vd} & 0 & K_{pd} & 0 & 0 \\ M_{ud} & 0 & M_{wd} & 0 & M_{qd} & 0 \\ 0 & N_{vd} & 0 & 0 & 0 & N_{rd} \end{bmatrix}. \quad (3)$$

<sup>1</sup>The use of such models is more common in other fields, such as aircraft<sup>6,7</sup>.

The relevant parameters in formula 3 are explained as follows:  $m$  is the mass of the UUV,  $z_g$  represents the offset of the center of gravity on the  $Z$ -axes,  $I_x, I_y, I_z$  are the moments of inertia about the  $X, Y, Z$ -axes.  $X_{ud}, X_{qd}$  are the added mass on the  $X$ -axes caused by the acceleration in the  $u$  direction and the angular acceleration in the  $q$  direction.  $Y_{vd}, Y_{pd}, Y_{rd}$  are the added mass on the  $Y$ -axes caused by the acceleration in the  $v$  direction and the angular acceleration in the  $p$  and  $r$  direction.  $Z_{wd}, Z_{qd}$  are the added mass on the  $Z$ -axes caused by the acceleration in the  $w$  direction and the angular acceleration in the  $q$  direction.  $K_{vd}, K_{pd}$  are the added moments of inertia in the  $K$  direction caused by the acceleration in the  $v$  direction and the angular accelerations in the  $p$  direction.  $M_{ud}, M_{wd}, M_{qd}$  are the added moments of inertia in the  $M$  direction caused by the acceleration in the  $u$  direction and the angular accelerations in the  $w$  and  $q$  directions.  $N_{vd}, N_{rd}$  are the added moments of inertia in the  $N$  direction caused by the acceleration in the  $v$  direction and the angular accelerations in the  $r$  direction.

The Coriolis term matrix  $\mathbf{C}(v)$  consists of two parts:

$$\mathbf{C}(v) = \mathbf{C}_a(v) + \mathbf{C}_{rb}(v), \quad (4)$$

where the  $\mathbf{C}_a(v)$  is the fluid dynamics Coriolis centripetal matrix and  $\mathbf{C}_{rb}(v)$  is the Lagrangian parameterization matrix, with each has the expression as:

$$\mathbf{C}_a(v) = \begin{bmatrix} 0 & 0 & 0 & 0 & -Z_{wd}w & Y_{vd}v \\ 0 & 0 & 0 & Z_{wd}w & 0 & -X_{ud}u \\ 0 & 0 & 0 & -Y_{vd}v & X_{ud}u & 0 \\ 0 & -Z_{wd}w & Y_{vd}v & 0 & -N_{rd}r & M_{qd}q \\ Z_{wd}w & 0 & -X_{ud}u & N_{rd}r & 0 & -K_{pd}p \\ -Y_{vd}v & X_{ud}u & 0 & -M_{qd}q & K_{pd}p & 0 \end{bmatrix}, \mathbf{C}_{rb}(v) = \begin{bmatrix} 0 & 0 & 0 & 0 & mw & -mv \\ 0 & 0 & 0 & -mw & 0 & mu \\ 0 & 0 & 0 & mv & -mu & 0 \\ 0 & mw & -mv & 0 & I_z r & -I_y q \\ -mw & 0 & mu & -I_z r & 0 & I_x p \\ mv & -mu & 0 & I_y q & -I_x p & 0 \end{bmatrix}. \quad (5)$$

The relevant parameters in formula 5 are explained as follows:  $u, v, w$  are the linear velocity along the  $X, Y, Z$ -axes.  $p, q, r$  are the angular velocity along the  $\phi, \theta, \psi$  directions.

The fluid dynamics damping matrix  $\mathbf{D}(v)$  is shown below:

$$\mathbf{D}(v) = \mathbf{D}_l(v) + \mathbf{D}_{nl}(v), \quad (6)$$

where the  $\mathbf{D}_l(v)$  is the linear term in the fluid dynamics damping matrix and  $\mathbf{D}_{nl}(v)$  is the nonlinear part. To simplify the exoression, we approximate the nonlinear part as zero matrix, so  $\mathbf{D}(v)$  is the same as  $\mathbf{D}_l(v)$ :

$$\mathbf{D}_l(v) = \begin{bmatrix} X_u & 0 & X_w & 0 & X_q & 0 \\ 0 & Y_v & 0 & Y_p & 0 & Y_r \\ Z_u & 0 & Z_w & 0 & Z_q & 0 \\ 0 & 0 & 0 & K_p & 0 & 0 \\ 0 & 0 & M_w & 0 & M_q & 0 \\ 0 & N_v & 0 & 0 & 0 & N_r \end{bmatrix}. \quad (7)$$

The relevant parameters in formula 7 are explained as follows:  $X_u, X_q, X_w$  are the fluid dynamics damping coefficients on the  $X$ -axes caused by the velocities in the  $u$  and  $w$  directions and the angular velocity in the  $q$  direction.  $Y_v, Y_p, Y_r$  are the fluid dynamics damping coefficients on the  $Y$ -axes caused by the velocity in the  $v$  direction and the angular velocities in the  $p$  and  $r$  directions.  $Z_u, Z_w, Z_q$  are the fluid dynamics damping coefficients on the  $Z$ -axes caused by the velocities in the  $u$  and  $w$  direction and the angular velocity in the  $q$  direction.  $K_p$  is the fluid dynamics damping coefficients about the  $K$  direction caused by the angular velocity in the  $p$  direction.  $M_w, M_q$  are the fluid dynamics damping coefficients about the  $M$  direction caused by the velocity in the  $w$  direction and the angular velocity in the  $q$  direction.  $N_v, N_r$  are the fluid dynamics damping coefficients about the  $N$  direction caused by the velocity in the  $v$  and the angular velocity in the  $r$  direction.

$\mathbf{g}(\eta)$  represents the received restoring force moment, and  $\mathbf{J}(\eta)$  is the velocity relationship change matrix between the hull coordinate system and the earth coordinate system. The expressions are listed as follows:

$$\mathbf{g}(\eta) = \begin{bmatrix} (W-B)\sin(\theta) \\ -(W-B)\cos(\theta)\sin(\phi) \\ -(W-B)\cos(\theta)\cos(\phi) \\ z_g W \cos(\theta) \sin(\phi) \\ z_g W \sin(\theta) \\ 0 \end{bmatrix}, \mathbf{J}(v) = \begin{bmatrix} \mathbf{R} & \mathbf{I} \\ \mathbf{I} & \mathbf{T} \end{bmatrix}, \text{ where } \mathbf{T} = \begin{bmatrix} 1 & \sin(\phi)\tan(\theta) & \cos(\phi)\tan(\theta) \\ 0 & \cos(\phi) & -\sin(\phi) \\ 0 & \sin(\phi)/\cos(\theta) & \cos(\phi)\cos(\theta) \end{bmatrix}, \quad (8)$$

$$\mathbf{R} = \begin{bmatrix} \cos(\psi)\cos(\theta) & -\sin(\psi)\cos(\phi) + \sin(\phi)\sin(\theta)\cos(\psi) & \sin(\psi)\sin(\phi) + \sin(\theta)\cos(\psi)\cos(\phi) \\ \sin(\psi)\cos(\theta) & \cos(\psi)\cos(\phi) + \sin(\phi)\sin(\theta)\sin(\psi) & -\cos(\psi)\sin(\phi) + \sin(\theta)\sin(\psi)\cos(\phi) \\ -\sin(\theta) & \sin(\phi)\cos(\theta) & \cos(\phi)\cos(\theta) \end{bmatrix}.$$

The relevant parameters in formula 8 are explained as follows:  $W, B$  are the gravity and buoyancy on UUV.  $\psi, \theta, \varphi$  are the roll, pitch and yaw angles of UUV.

**Table 1.** Specific model parameters of actual UUV

Parameter	Value	Unit	Parameter	Value	Unit	Parameter	Value	Unit
$m$	4825	$kg$	$Z_g$	0.04	$meter$	$I_x$	947	$kg \cdot m^2$
$I_y$	15531	$kg \cdot m^2$	$I_z$	16063	$kg \cdot m^2$	$X_{ud}$	-323.568	-
$X_{qd}$	241.704	-	$Y_{vd}$	4891.9	-	$Y_{pd}$	349.92	-
$Y_{rd}$	1391.9	-	$Z_{wd}$	6279.4	-	$Z_{qd}$	2801.3	-
$K_{vd}$	382.968	-	$K_{pd}$	-264.384	-	$M_{ud}$	249.48	-
$M_{wd}$	-2683.4	-	$M_{qd}$	-128270	-	$N_{vd}$	1264.9	-
$N_{rd}$	7811	-	$X_u$	-9738	-	$X_w$	1964.5	-
$X_q$	12944	-	$Y_v$	-45799.6	-	$Y_p$	16681	-
$Y_r$	395180	-	$Z_u$	4705.4	-	$Z_w$	-40849.4	-
$Z_q$	-568187	-	$K_p$	-71180	-	$M_w$	-303345	-
$M_q$	-9096830	-	$N_v$	199295	-	$N_r$	-6183830	-
$W$	47285	$N$	$B$	47285	$N$			

We next present the specific parameters of the UUV used in the experiment. The UUV is designed for underwater optical cable-laying tasks, and the context for this dataset involves the UUV's hovering anti-interference task, which is influenced by horizontal, non-rotating ocean currents, as depicted in Figure 2 of the main text. In order to unify and simplify the table format, we do not list the units of each parameter. The specific parameters are provided in Table 1.

## S.2 Preliminary knowledge of SMC (Sliding mode Control)

Consider a discrete UUV system in model 1. Due to the influence of changes in the orientation and velocity of the UUV on system matrices like  $\mathbf{M}(\mathbf{v}_k)$ , coupled with the current disturbance, the system exhibits strong nonlinear characteristics and is highly disturbed. This can lead to the failure of certain control strategies to stabilize the system. To achieve good control accuracy with the nonlinear model under the influence of disturbance  $\delta_k$ , a sliding mode controller is introduced to stabilize the UUV model.

Design the following sliding surface constraining both position deviation and speed deviation:

$$\mathbf{s}_{\delta,k} = \mathbf{c}\mathbf{v}_{\delta,k} + \boldsymbol{\eta}\delta_k, \quad (9)$$

where  $\mathbf{s}_k$  is the weight to balance whether to focus more on the deviation on position or speed. With a sign function  $\mathbf{s} = -\rho \text{sgn}(\mathbf{s})$  play as the reaching law of SMC, and formulate its discrete form:

$$\frac{\mathbf{s}_{\delta,k+1} - \mathbf{s}_{\delta,k}}{dt} = -\rho \text{sgn}(\mathbf{s}_{\delta,k}). \quad (10)$$

Substitute the discrete model information and 9 into equation 10 and simplify them, we can get:

$$\boldsymbol{\tau}_{\delta,k} = \mathbf{C}(\mathbf{v}_k)\mathbf{v}_{\delta,k} + \mathbf{D}(\mathbf{v}_k)\mathbf{v}_{\delta,k} + \mathbf{g}(\boldsymbol{\eta}_k) - \mathbf{M}(\mathbf{v}_k)\mathbf{c}^{-1}\mathbf{J}\mathbf{v}_{\delta,k} - \mathbf{M}\mathbf{c}^{-1}\rho \text{sgn}(\mathbf{s}_{\delta,k}). \quad (11)$$

Thus, the sliding mode control law for the UUV is derived. Under this control strategy, the sliding mode state will eventually converge to the vicinity of the sliding mode surface  $\mathbf{s}_{\delta,k} = 0$  within a boundary  $\Delta$  and remain there indefinitely<sup>9</sup>. Specifically,  $|\mathbf{s}_{\delta,k}| \leq \Delta$  for all  $k > k^*$ , where  $k^*$  is a constant. To determine the specific value of  $\Delta$ , we substitute 11 and 10 into the UUV model and simplify the resulting expression:

$$\mathbf{s}_{\delta,k+1} = \mathbf{s}_{\delta,k} - \rho \text{sgn}(\mathbf{s}_{\delta,k})dt + \mathbf{c}\mathbf{M}(\mathbf{v}_k)^{-1}\boldsymbol{\delta}_k dt. \quad (12)$$

As  $\mathbf{s}_{\delta,k}$  eventually approaches zero, the bias between  $\mathbf{s}_{\delta,k}$  and  $\mathbf{s}_{\delta,k+1}$  arises from the disturbance  $\boldsymbol{\delta}_k$  and the thrust  $\boldsymbol{\tau}_{\delta,k}$ , which compensates for the previous disturbance  $\boldsymbol{\delta}_{k-1}$ . Therefore, it can be concluded that once the conditions mentioned above are met, the sliding mode surface  $\mathbf{s}_{\delta,k}$  will be bounded within  $\Delta$ , where  $\Delta = \rho \text{sgn}(\mathbf{s}_{\delta,k}) + \mathbf{c}\mathbf{M}^{-1}\boldsymbol{\delta}_k dt$ . This ensures that the system will remain stable.

### S.3 Preliminary knowledge of LQR (Linear Quartic Optimal Control)

In this subsection, a brief introduction to LQR is given. As formulated in the paper, the linear discrete model of the UUV's hovering task has been obtained as:

$$\mathbf{x}_{k+1} = \mathbf{A}_k \mathbf{x}_k + \mathbf{B}_k \tau_k + \delta_k + \mathbf{w}_k, \quad (13)$$

where the terms have the same meaning as those in the paper. For ease of understanding, we reproduce the expression for the system matrix  $\mathbf{A}_k$ , the input matrix  $\mathbf{B}_k$ , and other definitions in Remark 2.

$$\mathbf{A}_k = \begin{bmatrix} \left( \frac{\partial \mathbf{J}(\eta_0) \mathbf{v}_0}{\partial \eta_0} + \mathbf{I} \right) dt & \mathbf{J}(\eta_0) dt \\ -\frac{\partial \mathbf{M}(\mathbf{v}_0)^{-1} \mathbf{g}(\eta_0)}{\partial \eta_0} dt & [\mathbf{I} - \frac{\partial \mathbf{H}(\mathbf{v}_0, \tau_0)}{\partial \mathbf{v}_0}] dt \end{bmatrix}, \mathbf{B}_k = \begin{bmatrix} 0 & \frac{\partial \mathbf{M}(\mathbf{v}_0)^{-1} \tau_0}{\partial \tau_0} dt \end{bmatrix}^T, \quad (14)$$

$$\mathbf{H}(\mathbf{v}_0, \tau_0) = \mathbf{M}(\mathbf{v}_0)^{-1} \mathbf{C}(\mathbf{v}_0) \mathbf{v}_0 + \mathbf{M}(\mathbf{v}_0)^{-1} \mathbf{D}(\mathbf{v}_0) \mathbf{v}_0 + \mathbf{M}(\mathbf{v}_0)^{-1} \mathbf{g}(\eta_0) - \mathbf{M}(\mathbf{v}_0)^{-1} \tau_0.$$

**Remark 2**  $\eta_0$ ,  $\mathbf{v}_0$ , and  $\tau_0$  represent the values of  $\eta$ ,  $\mathbf{v}$ , and  $\tau^\delta$  at the time step  $k = 0$ , respectively.  $\mathbf{I}$  is the identity matrix with the same dimensions as  $\mathbf{J}(\eta_k)$ .  $\mathbf{H}(\mathbf{v}_0, \tau_0)$  is an intermediate variable introduced to simplify the notation.  $\mathbf{x}_k$  and  $\tau_k$  represent the system state and thrust input of the mismatched model, respectively. Their physical meanings are identical to those of  $\mathbf{x}_k^\delta$  and  $\tau_{\delta,k}$ . The only distinction is that, in contrast to model (1), random noise  $\mathbf{w}_k$  from the thrusters is introduced. The remaining terms are consistent with those in model (1).

The former strategy, SMC, tends to provide high-gain input with high-frequency oscillations, which is known as "chattering". This can cause excessive wear and tear on actuators and degrade the performance of the control system while increasing the control consumption. To reach the balance between control accuracy and consumption, a  $H_2$  controller is designed to carry out the task. But since it works for system without disturbance, we need to first simplify the UUV model as:

$$\mathbf{x}_{\varepsilon,k+1} = \mathbf{A}_k \mathbf{x}_{\varepsilon,k} + \mathbf{B}_k \tau_{\varepsilon,k} + \mathbf{w}_k, \quad (15)$$

where  $\mathbf{x}_{\varepsilon,k}$  and  $\tau_{\varepsilon,k}$  stand for the deviation state and thrust when the system is not influenced by current disturbance. The rest terms remain the same as the actual model 13.

$$\begin{cases} J_k^* = \min_{\tau_k} \left[ (\mathbf{x}_{\varepsilon,k}^T \mathbf{Q} \mathbf{x}_{\varepsilon,k} + \tau_k^T \mathbf{R} \tau_k) + \mathbf{x}_{k+1}^T \mathbf{P}_{k+1} \mathbf{x}_{k+1} \right], \\ \tau_k^* = \min_{\tau_k} \{ J_{\varepsilon,k} + [\mathbf{x}_{k+1}^T \mathbf{P}_{k+1} \mathbf{x}_{k+1} - \mathbf{x}_{\varepsilon,k+1}^T \mathbf{P}_{k+1} \mathbf{x}_{\varepsilon,k+1}] \}. \end{cases} \quad (16)$$

$$J_k = \mathbf{x}_{k+1}^T \mathbf{P}_{k+1} \mathbf{x}_{k+1}, J_{\varepsilon,k} = \mathbf{x}_{\varepsilon,k+1}^T \mathbf{P}_{k+1} \mathbf{x}_{\varepsilon,k+1}, \quad (17)$$

Define the cost function as  $F = \mathbf{x}_k^T \mathbf{Q} \mathbf{x}_k + \tau_k^T \mathbf{R} \tau_k$ , and solve a QP(Convex Quadratic Programming) problem using the Riccati equation<sup>10</sup>. We can get the feedback control law as:

$$\tau_k^* = -\mathbf{K}_\varepsilon \mathbf{x}_k, \quad (18)$$

$$\mathbf{K}_\varepsilon = -(\mathbf{R} + \mathbf{B}_k^T \mathbf{P}_{k+1} \mathbf{B}_k)^{-1} \mathbf{B}_k^T \mathbf{P}_{k+1} \mathbf{A}_k, \quad (19)$$

where  $\mathbf{K}_\varepsilon$  is the optimal control gain and  $\mathbf{P}_k$  satisfies a discrete algebra Riccati equation (ARE)

$$\mathbf{P}_k = \mathbf{A}_k^T \mathbf{P}_{k+1} \mathbf{A}_k - \mathbf{A}_k^T \mathbf{P}_{k+1} \mathbf{B}_k (\mathbf{R} + \mathbf{B}_k^T \mathbf{P}_{k+1} \mathbf{B}_k)^{-1} \mathbf{B}_k^T \mathbf{P}_{k+1} \mathbf{A}_k + \mathbf{Q} \quad (20)$$

### S.4 Performance comparison under stable ocean current disturbance

This section focuses on the influence of a stable ocean current during the UUV hovering mission, as depicted in Fig. 1. The stable ocean current is modeled as a continuous, directed seawater flow, consisting of a constant current component superimposed with Gaussian white noise. The initial pose of the UUV is set to  $(45, 45, 110, 0, 0, 0)^T$ , while the target hovering pose is defined as  $(50, 50, 100, 0, 0, 0)^T$ . It is assumed that the stable ocean current disturbance impacts the system at the 1000th step, whereas thruster noise persists throughout the operation. To demonstrate the effectiveness and superiority of the proposed COC algorithm, the control performance of SMC and LQR is evaluated under the parameter settings  $\mathbf{R} = \mathbf{I}$ ,  $\mathbf{Q} = 100\mathbf{I}$ , and  $z = 2$ .

The thrusts computed by LQR, SMC, and COC are applied to the UUVs, and Fig. 2 illustrates the deviations between actual and desired poses. Consistent with the main conclusions, COC effectively integrates SMC's advantages, leveraging high-frequency thrust adjustments to rapidly guide the UUV toward the target state under stable ocean current disturbances.

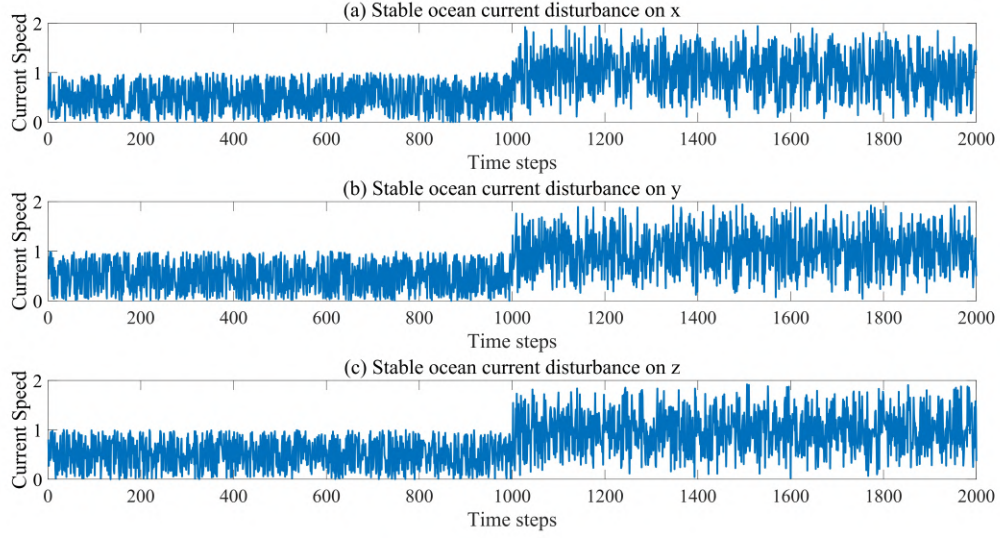


**Figure 1. Disturbances of ocean current.** Subfigure (a) presents the ocean current disturbance on x (b) shows the ocean current disturbance on y. Meanwhile, Subfigure (c) depicts the ocean current disturbance on z.

During the first 530 time steps, the gray lines converge to the desired pose (zero in this experiment) faster and more accurately than the blue lines, demonstrating COC's superior convergence speed and steady-state accuracy over LQR. Between time steps 650 and 1000, the gray lines remain closer to the setpoint, highlighting LQR's larger steady-state error. Although SMC nearly eliminates this error, Fig. 2(f) shows it introduces persistent oscillations. The COC framework overcomes these limitations by maintaining smoother trajectories with lower oscillation amplitude than SMC and smaller pose deviations than LQR. After 1000 time steps, the gray and red lines stay closer to the desired state than the blue lines, confirming that both SMC and COC outperform LQR in steady-state accuracy. However, SMC exhibits occasional peaks and oscillations, while COC effectively mitigates overshoot, ensuring stable control. In summary, the deviation separation mechanism in COC dynamically balances LQR and SMC, suppressing overshoot and enhancing robustness and precision in dynamic, uncertain environments.

As discussed in the main text, the effectiveness of the COC framework depends largely on the deviation separation mechanism. To illustrate its impact, Fig. 3 presents the separated sub-deviations, which follow similar trends to those in the main analysis.

From the start to the 175th step, the purple region dominates, indicating that current disturbance is the primary source of deviation. This results from the initial state deviation, causing the COC algorithm to rely mainly on SMC. Between steps 650 and 1000, the deviation decreases significantly as all three controllers stabilize. After 1000 steps, the total deviation increases, primarily due to the growing pink segment, representing thruster noise-induced deviation. This fluctuation follows a cyclical pattern, where the dominance of one deviation diminishes while the other becomes more pronounced. Throughout this process, the UUV's pose accuracy is iteratively refined, and thruster consumption is efficiently managed, preventing unnecessary power expenditure. This adaptive response highlights the COC framework's effectiveness in maintaining optimal control performance despite environmental disturbances.

The thrust curves of eight thrusters under LQR, SMC, and COC control strategies are shown in Fig. 4. During the initial 300 steps, SMC (red lines) exhibits significant overshoot and oscillation due to aggressive thrust output, leading to saturation. In contrast, COC moderates thrust, avoiding extreme values seen in SMC, though with a slightly longer stabilization period (within 200 steps). Later, both SMC and COC maintain high-frequency oscillations, while LQR (blue line) applies smaller thrust, indicating weaker disturbance suppression. After 550 steps, COC stabilizes with lower thrust and minimal oscillations, achieving high accuracy with reduced thrust consumption by shifting toward LQR dominance. Beyond 1000 steps, when the stable ocean current occurs, both COC and SMC exhibit intensified oscillations. Consistent with the main paper, COC maintains control accuracy while selecting a smoother, lower-magnitude thrust profile, effectively reducing thruster wear and enhancing overall performance.

Fig. 5 presents a comparative analysis of the overall performance of the three control strategies. The control cost is computed as the same way in the body text, with the logarithm  $\log_{10}$  applied for better visualization. As shown in Fig. 5, COC's control cost in the first segments exceeds that of LQR but remains lower than SMC, as it stabilizes the UUV using high-frequency



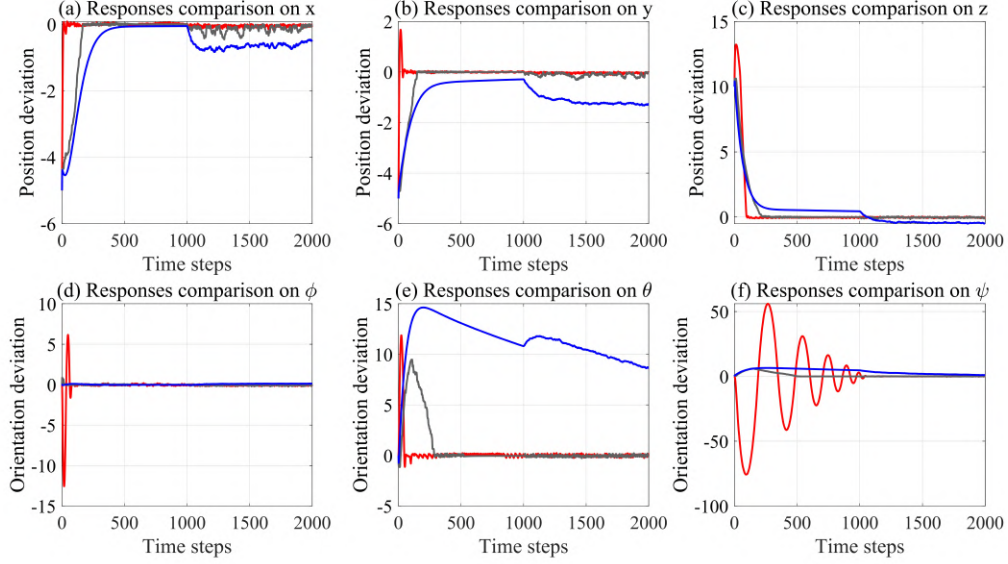


**Figure 2. Deviation responses of UUV under ocean current disturbance with different controllers.** (a) illustrates the state response of position  $x$ , while (b) depicts the state response of position  $y$  and (c) presents the state response of position  $z$ . (d), (e), and (f) shows the state response of orientation  $\phi$ ,  $\theta$ , and  $\psi$ , respectively. The ocean current disturbance is introduced at the 1000th step in all subfigures. The blue, red, and gray lines represent the deviation responses under the LQR, SMC, and COC control strategies.

thrust adjustments with lower amplitude than SMC. During the next time, as deviations converge, COC consistently achieves the lowest control cost, demonstrating its ability to maintain high accuracy with minimal control effort. These results further validate the effectiveness of COC's collaborative control strategy.

## S.5 Performance comparison under increasing current disturbance

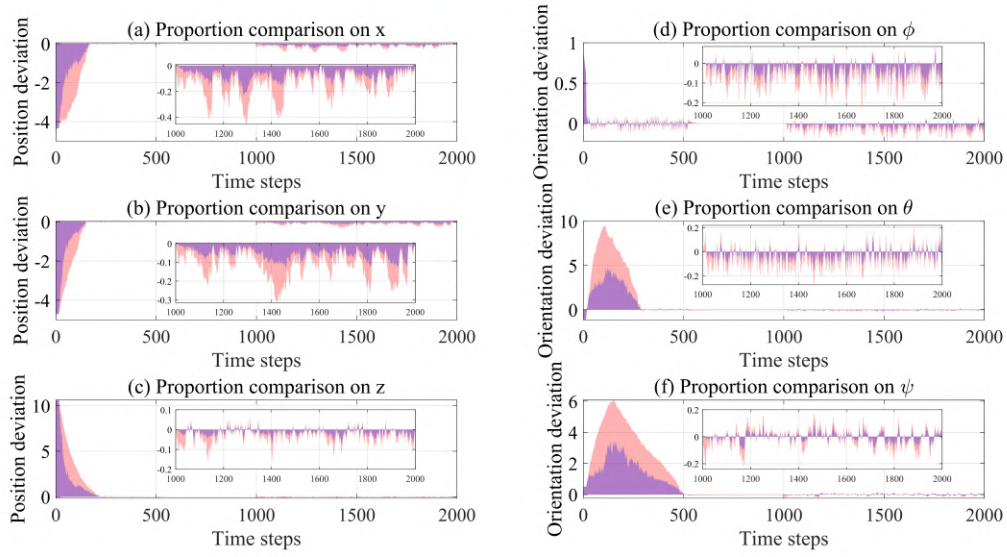
This section investigates the impact of an increasing ocean current disturbance, as depicted in Fig. 6. The disturbance progressively intensifies over time, reaching twice its original magnitude between steps 1000 and 2000. All other experimental conditions remain consistent with those in the stable ocean current scenario.

Fig. 7 shows the deviations between actual and desired poses under LQR, SMC, and COC control. While the trends align with the main paper's conclusions, this analysis highlights COC's ability to maintain stability even when a sub-controller becomes ineffective.

During the initial 1000 time steps, the trajectories of all three control strategies exhibit similar trends to those observed in the stable ocean current case. However, after step 1000, as the ocean current disturbance increases, distinct differences begin to emerge. At the onset of the anti-disturbance phase (between steps 1000 and 1300), the disturbance remains within the tolerance bounds of the SMC controller. Consequently, the red curve (representing SMC) remains closest to the desired pose, with COC as the second-best performer. However, as illustrated in Fig. 7 (a) and (b), as the disturbance magnitude further increases, it exceeds the suppression capability of SMC. Once this threshold is surpassed, the SMC controller fails to compensate effectively, leading to the divergence of the red curve.

In contrast, the LQR controller, due to its static feedback structure, inherently possesses a more considerable stability margin. Although the increasing disturbance results in a more significant steady-state error for LQR, it does not cause divergence. By leveraging the deviation separation mechanism, the COC framework effectively limits the proportion of disturbance impact assigned to the SMC sub-controller, thereby reducing the tendency of SMC to diverge. Simultaneously, the LQR sub-controller is more prominent in counteracting the disturbance. As a result, COC successfully integrates the advantages of LQR, benefiting from its enhanced stability margin. This enables COC to maintain stability even under disturbances that exceed the upper operational limit of the SMC sub-controller, further demonstrating the robustness and adaptability of the proposed framework.

As in the main text, the effectiveness of the COC framework is highly dependent on the deviation separation mechanism. Fig. 7 illustrates the separated sub-deviations, which generally follow similar trends to those observed in the primary analysis, except for the period between steps 1300 and 2000. As shown in Fig. 8 (a) and (b), during this period, the increasing disturbance exceeds the upper limit of the SMC sub-controller, causing a rapid increase in the total deviation, with the purple



**Figure 3. Comparison of the proportion of sub-deviations under ocean current disturbance.** (a), (b), (c) and (d), (e), (f) are the proportion comparison of position  $x$ ,  $y$ ,  $z$  and orientation  $\phi$ ,  $\theta$ , and the  $\psi$ , respectively. The pink part represents the sub-deviation from thruster noise and the purple part represents that current disturbance.

region becoming dominant. However, when the disturbance reaches its maximum level (twice the magnitude of the original disturbance), the proportions of the pink and purple regions stabilize at approximately equal levels. This confirms that the deviation separation mechanism effectively limits the portion of the deviation assigned to the SMC sub-controller, thereby ensuring system stability.

The thrust curves of the eight thrusters under LQR, SMC, and COC control strategies are presented in Fig. 9. The overall trends are mainly consistent with those observed in the main text, with notable differences arising after the 1300th time step. Specifically, when the disturbance surpasses the tolerance limit of the SMC sub-controller, the thrust outputs under COC exceed those of both SMC and LQR. However, once the disturbance peaks, the COC thrust values return to similar levels observed under standard ocean current disturbances.

Fig. 10 provides a comparative analysis of the overall performance of the three control strategies. The control cost is computed using the same methodology as in the main text, with a logarithmic transformation ( $\log_{10}$ ) applied for improved visualization. The results indicate a similar trend to that of the main text, with one key distinction: when the disturbance exceeds the limit of SMC, the control cost of COC temporarily surpasses that of LQR due to the divergent behavior of the SMC sub-controller.

In summary, this section highlights that the system becomes unstable under SMC alone when ocean currents exceed the SMC sub-controller's stability threshold. In contrast, COC continues to oscillate but remains convergent, closely aligning with LQR's control performance. This indicates that COC effectively mitigates the divergence observed in SMC. This robustness is attributed to COC's collaborative mechanism, in which the LQR component constrains the thrust output when SMC exhibits a divergent trend, thereby preventing extreme instability.

## S.6 Performance comparison under loading change situation

This section examines the effects of load variations on the control performance of the UUV. As illustrated in Fig. 11, the overall disturbance consists of thruster noise, which follows a Gaussian white noise distribution, and the load-changing disturbance. The UUV's mass gradually increases between steps 667 and 1327—accounting for one-third of the total simulation period—before experiencing a sudden decrease. This load variation simulates a common scenario in which the UUV releases payloads during an underwater mission. All other experimental conditions remain consistent with those in the stable ocean current scenario.

Fig. 12 presents the deviations between actual and desired poses under LQR, SMC, and COC control strategies. The overall trends align with the conclusions of the main text: COC effectively manages all six states of deviation, whereas SMC exhibits severe oscillations (particularly evident in Fig. 12 (f)), and LQR demonstrates slow convergence (as observed in Fig. 12 (e)). However, a key difference emerges from the results in the main text. In Fig. 12 (a), (b), (c), and (d), the steady-state deviations (gray lines) under load-changing conditions are more minor than those observed under ocean current disturbances. This finding

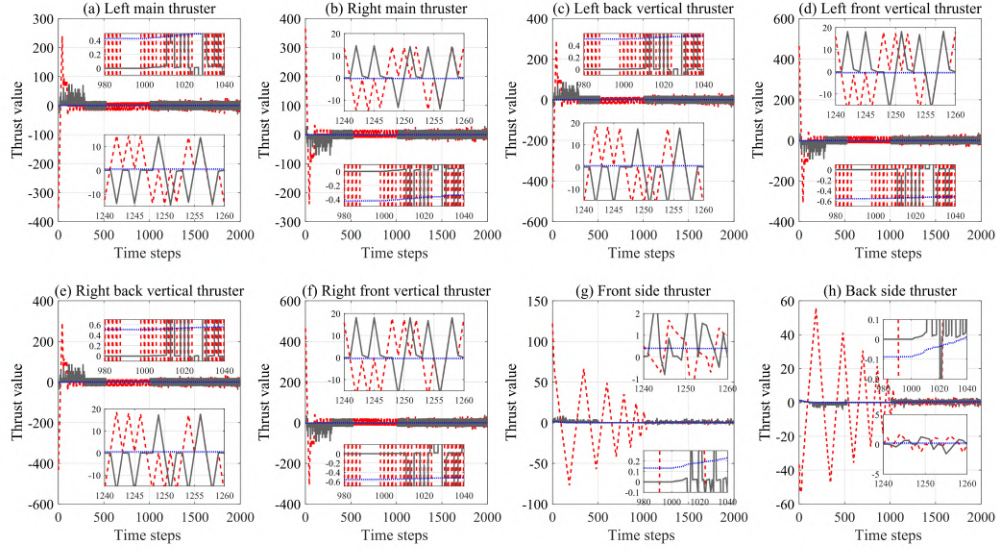


**Figure 4. Thrust variations of each thruster under the influence of ocean current disturbance.** (a) represents the thrust variation of the left-main thruster. (b) illustrates the thrust variation of the right-main thruster. (c) shows the thrust variation of the left-back vertical thruster. (d) displays the thrust variation of the left-front vertical thruster. (e) presents the thrust variation of the right-rear vertical thruster. (f) demonstrates the thrust variation of the right-front vertical thruster. (g) captures the thrust variation of the front-side thruster. (h) delineates the thrust variation of the rear-side thruster. The thrust profiles are represented by blue, red, and gray lines corresponding to LQR, SMC, and COC, respectively.

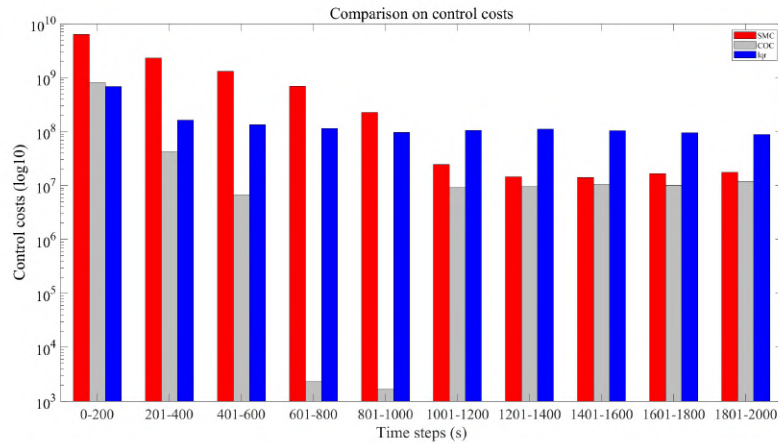
suggests that COC effectively compensates for the model uncertainty introduced by load variations, ensuring that no specialized control strategy is required for UUV operations under varying loads.

Fig. 13 illustrates the separated sub-deviations, which generally follow trends similar to those in the primary analysis, except for the period between time steps 1300 and 2000. During this period, COC's strong ability to mitigate model mismatches results in a tiny total deviation, which is nearly imperceptible in Fig. 13. In summary, the separated sub-deviation curves further validate COC's capability to compensate for load-changing disturbances effectively.

The thrust curves of the eight thrusters under LQR, SMC, and COC control strategies are shown in Fig. 14. During the first 1000 time steps, the thrust trends remain consistent with those in the main text. However, a notable distinction emerges once the load-changing disturbance affects the system. Unlike the continuous fluctuations observed in previous scenarios, the thrust outputs under COC closely align with those of LQR. This phenomenon indicates that, when faced with model parameter uncertainties, COC maintains precise control performance with a minimal increase in thrust.

To further validate these findings, Fig. 15 presents a comparative analysis of the overall control performance of the three strategies. The control cost is computed using the same methodology as in the main text, with a logarithmic transformation ( $\log_{10}$ ) applied for improved visualization. The time steps 600–2000 results indicate that COC effectively minimizes control costs compared to LQR and SMC. Specifically, the slow convergence of LQR results in a persistently high cost associated with control accuracy, while the oscillatory nature and high-gain thrust of SMC lead to a considerable control cost. Consequently, since COC achieves control accuracy comparable to that of SMC while maintaining a control effort similar to that of LQR, it emerges as the optimal control strategy in this scenario.





**Figure 5. Histogram of control costs for different controllers under ocean current disturbance.** The control process is discretized into ten segments, each comprising 200 time steps. The red, gray, and blue cuboids represent the logarithm of each controller's cost function.

## References

1. Fossen, T. I. *Guidance and control of ocean vehicles* (1999).
2. Gertler, M. & Hagen, G. R. Standard equations of motion for submarine simulation. Tech. Rep. (1967).
3. Prestero, T. T. J. *Verification of a six-degree of freedom simulation model for the REMUS autonomous underwater vehicle*. Ph.D. thesis, Massachusetts institute of technology (2001).
4. Kim, J., Kim, K., Choi, H., Seong, W. & Lee, K.-Y. Depth and heading control for autonomous underwater vehicle using estimated hydrodynamic coefficients. In *MTS/IEEE Oceans 2001. An Ocean Odyssey. Conference Proceedings (IEEE Cat. No. 01CH37295)*, vol. 1, 429–435 (IEEE, 2001).
5. Li, J. H., Lee, P. M. & Jun, B. H. Application of a robust adaptive controller to autonomous diving control of an auv. In *30th Annual Conference of IEEE Industrial Electronics Society, 2004. IECON 2004*, vol. 1, 419–424 (IEEE, 2004).
6. Mitchell, D. G. & Hoh, R. H. Low-order approaches to high-order systems: Problems and promises. *J. Guid. Control. Dyn.* **5**, 482–489 (1982).
7. Hodgkinson, J. Equivalent systems criteria for handling qualities of military aircraft. *1982. 11* (1982).
8. Petrich, J. & Stilwell, D. J. Model simplification for auv pitch-axis control design. *Ocean. Eng.* **37**, 638–651 (2010).
9. Ma, H., Wu, J. & Xiong, Z. Discrete-time sliding-mode control with improved quasi-sliding-mode domain. *IEEE Transactions on Ind. Electron.* **63**, 6292–6304 (2016).
10. Tijjani, A. S., Chemori, A. & Creuze, V. A survey on tracking control of unmanned underwater vehicles: Experiments-based approach. *Annu. Rev. Control.* **54**, 125–147 (2022).

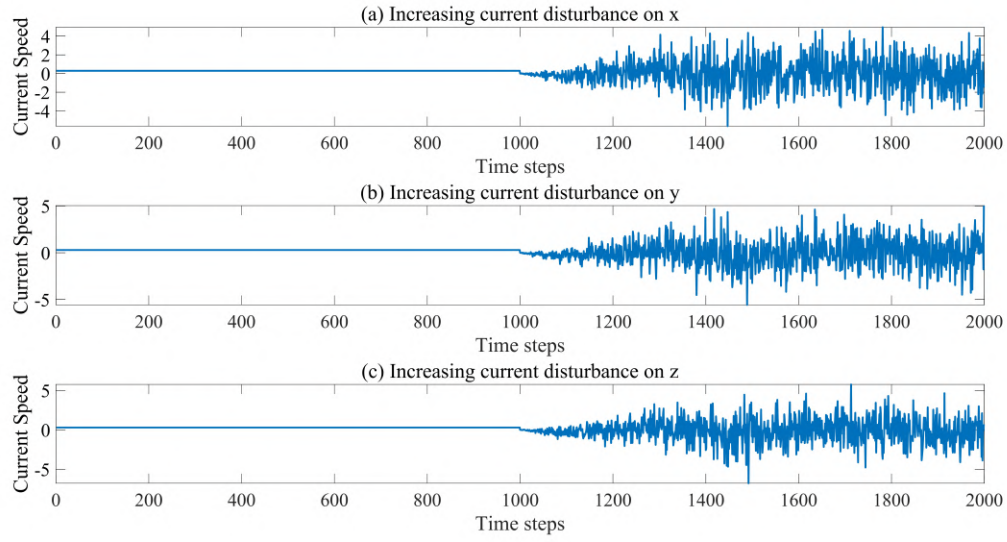


**Figure 6. Disturbances of increasing current.** Subfigure (a) presents the ocean current disturbance on x (b) shows the ocean current disturbance on y. Meanwhile, Subfigure (c) depicts the ocean current disturbance on z.

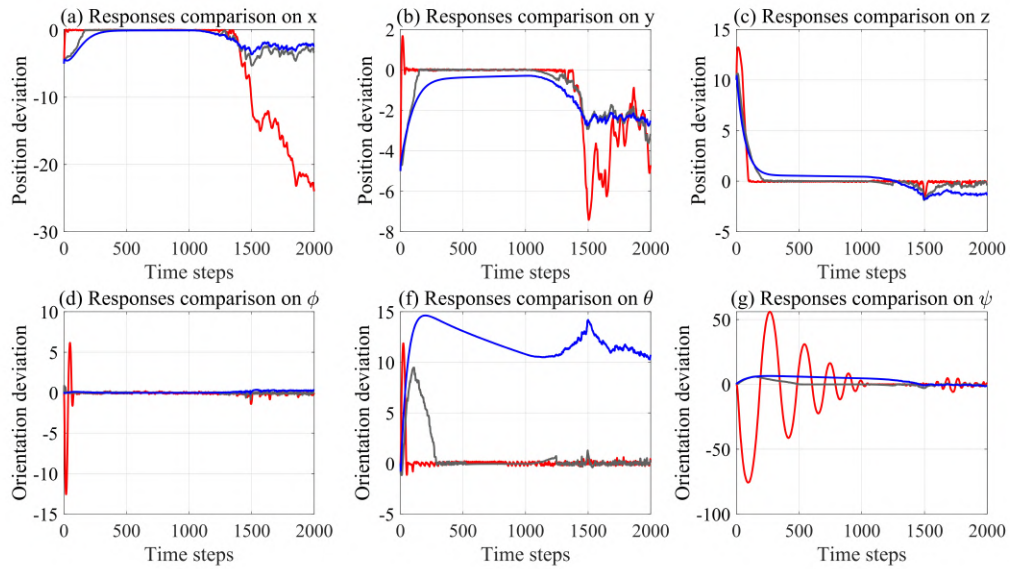


**Figure 7. Deviation responses of UUV under increasing current disturbance with different controllers.** (a) illustrates the state response of position x, while (b) depicts the state response of position y and (c) presents the state response of position z. (d), (e), and (f) shows the state response of orientation  $\phi$ ,  $\theta$ , and  $\psi$ , respectively. The ocean current disturbance is introduced at the 1000th step in all subfigures. The blue, red, and gray lines represent the deviation responses under the LQR, SMC, and COC control strategies.

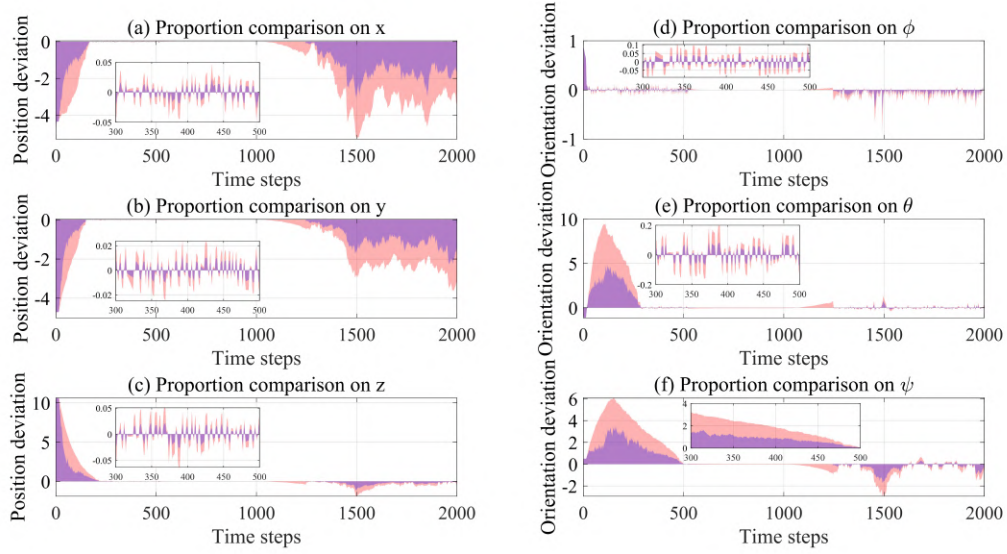


**Figure 8.** Comparison of the proportion of sub-deviations under increasing current disturbance. (a), (b), (c) and (d), (e), (f) are the proportion comparison of position  $x$ ,  $y$ ,  $z$  and orientation  $\phi$ ,  $\theta$ , and the  $\psi$ , respectively. The pink part represents the sub-deviation from thruster noise and the purple part represents that current disturbance.

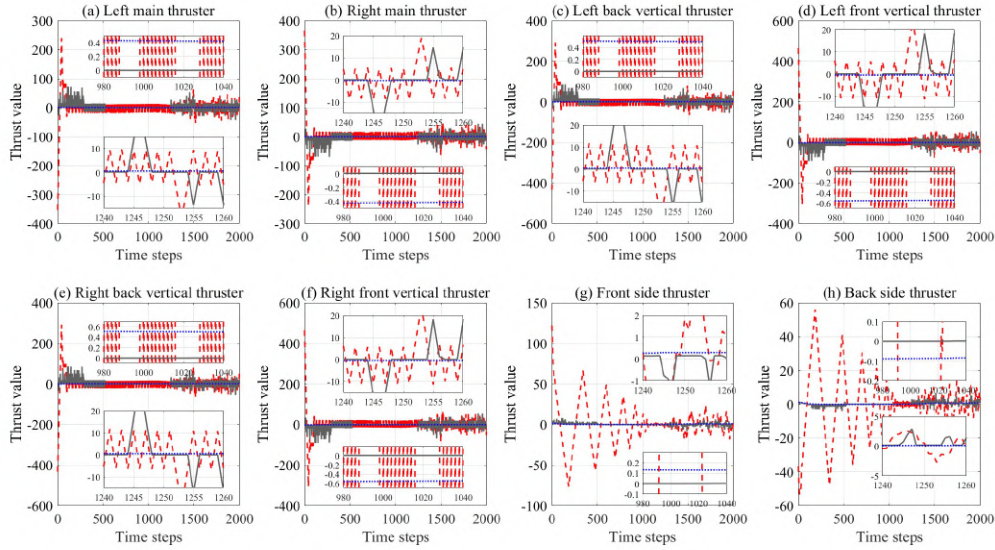


**Figure 9.** Thrust variations of each thruster under the influence of increasing current disturbance. (a) represents the thrust variation of the left-main thruster. (b) illustrates the thrust variation of the right-main thruster. (c) shows the thrust variation of the left-back vertical thruster. (d) displays the thrust variation of the left-front vertical thruster. (e) presents the thrust variation of the right-rear vertical thruster. (f) demonstrates the thrust variation of the right-front vertical thruster. (g) captures the thrust variation of the front-side thruster. (h) delineates the thrust variation of the rear-side thruster. The thrust profiles are represented by blue, red, and gray lines corresponding to LQR, SMC, and COC, respectively.

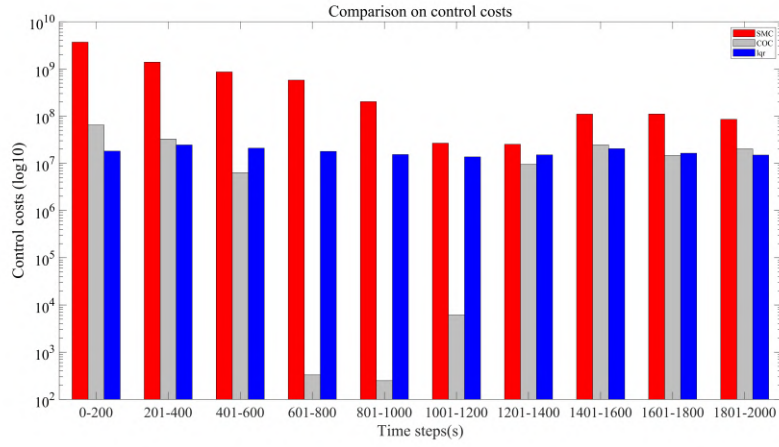


**Figure 10. Histogram of control costs for different controllers under increasing current disturbance.** The control process is discretized into ten segments, each comprising 200 time steps. The red, gray, and blue cuboids represent the logarithm of each controller's cost function.

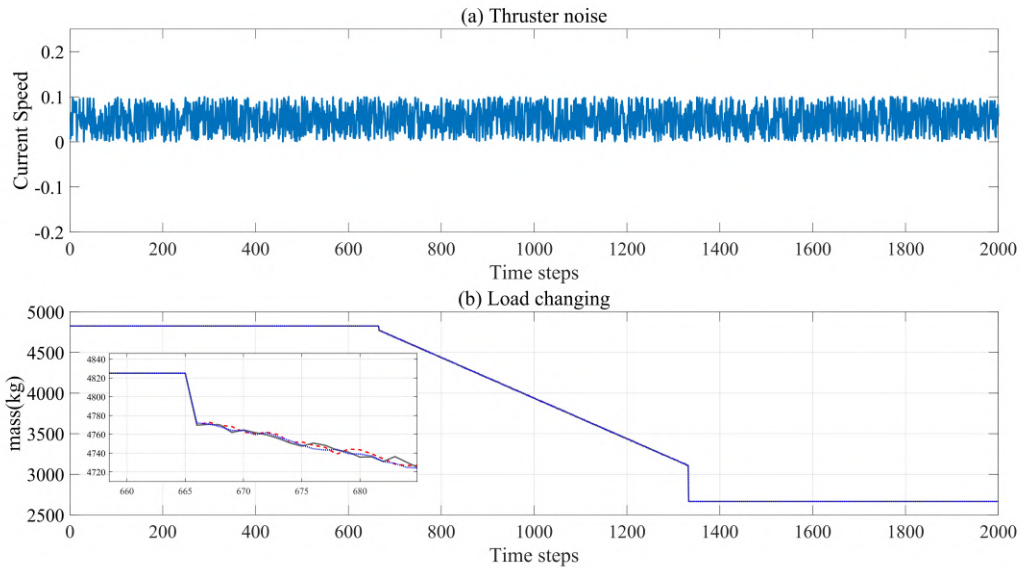


**Figure 11. Disturbances of load changing.** Subfigure (a) presents the curve of thruster noise and (b) shows the total mass of UUV during the load changing situations.



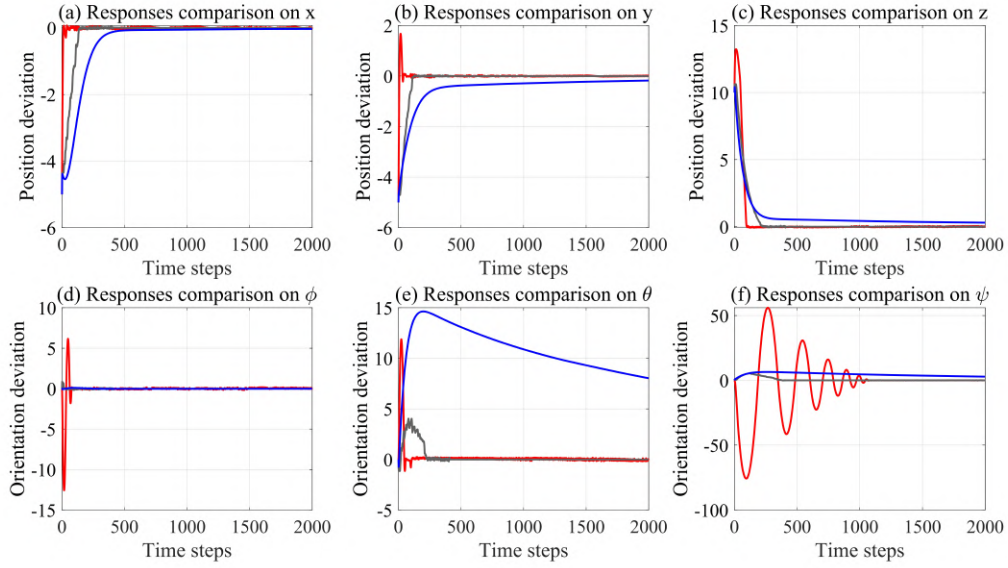


**Figure 12. Deviation responses of UUV under load changing disturbance with different controllers.** (a) illustrates the state response of position  $x$ , while (b) depicts the state response of position  $y$  and (c) presents the state response of position  $z$ . (d), (e), and (f) shows the state response of orientation  $\phi$ ,  $\theta$ , and  $\psi$ , respectively. The ocean current disturbance is introduced at the 1000th step in all subfigures. The blue, red, and gray lines represent the deviation responses under the LQR, SMC, and COC control strategies.

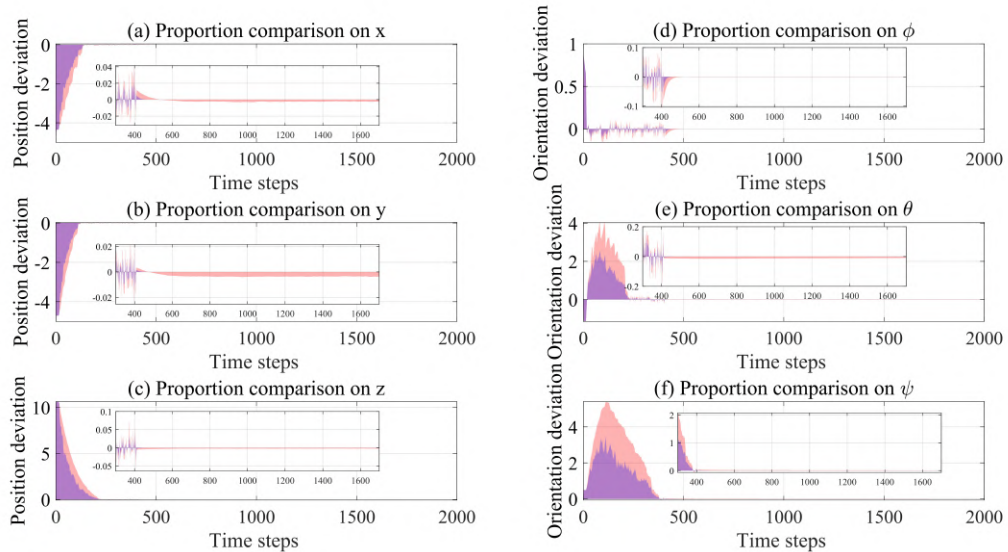


**Figure 13. Comparison of the proportion of sub-deviations under load changing disturbance.** (a), (b), (c) and (d), (e), (f) are the proportion comparison of position  $x$ ,  $y$ ,  $z$  and orientation  $\phi$ ,  $\theta$ , and the  $\psi$ , respectively. The pink part represents the sub-deviation from thruster noise and the purple part represents that current disturbance.



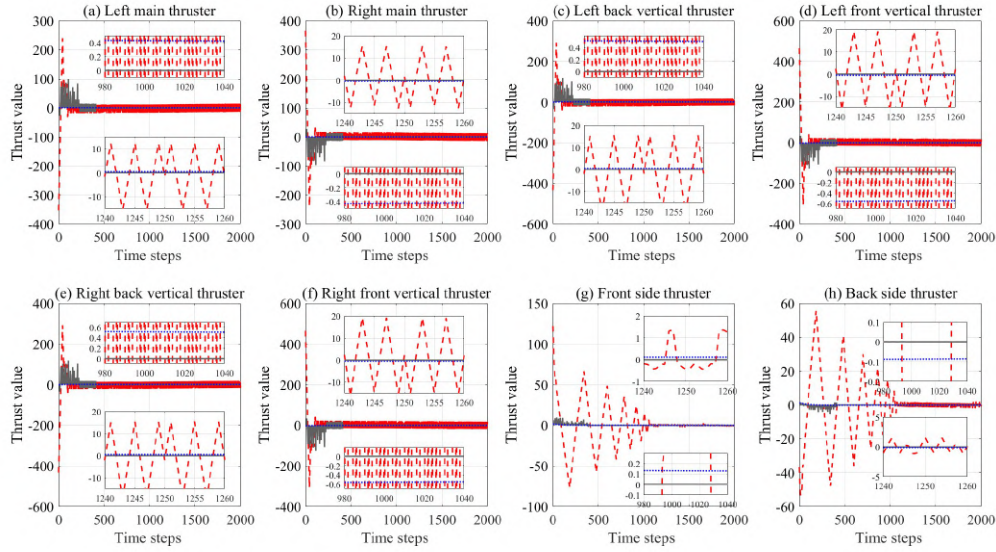


**Figure 14. Thrust variations of each thruster under the influence of load changing disturbance.** (a) represents the thrust variation of the left-main thruster. (b) illustrates the thrust variation of the right-main thruster. (c) shows the thrust variation of the left-back vertical thruster. (d) displays the thrust variation of the left-front vertical thruster. (e) presents the thrust variation of the right-rear vertical thruster. (f) demonstrates the thrust variation of the right-front vertical thruster. (g) captures the thrust variation of the front-side thruster. (h) delineates the thrust variation of the rear-side thruster. The thrust profiles are represented by blue, red, and gray lines corresponding to LQR, SMC, and COC, respectively.

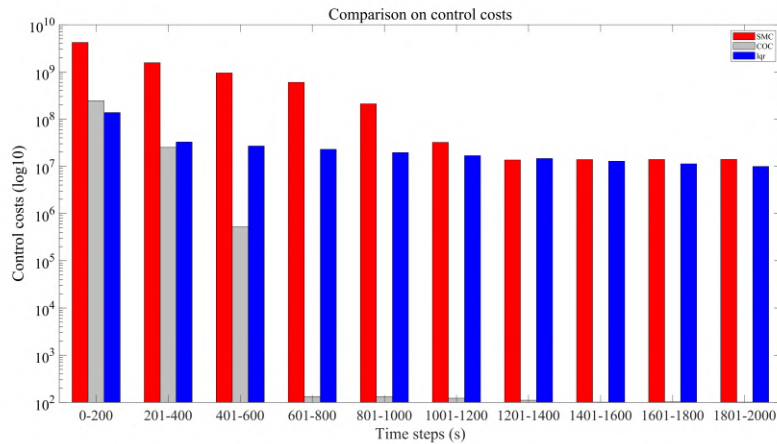


**Figure 15. Histogram of control costs for different controllers under load changing disturbance.** The control process is discretized into ten segments, each comprising 200 time steps. The red, gray, and blue cuboids represent the logarithm of each controller's cost function.